5. Probabilistic Method

5.1   PTHA Overview

5.1.1   *Previous PTHA studies*

Probabilistic tsunami hazard analysis (PTHA) is derived from and closely allied to probabilistic seismic hazard analysis (PSHA); the latter, developed originally by Cornell (1968) and subsequently described in several reports (including Senior Seismic Hazard Analysis Committee (SSHAC), 1997). Lin and Tung (1982), Rikitake (1988), and Downes and Stirling (2001) modified PSHA to develop a PTHA that calculates wave heights using a simple source specification. In a related effort, a recent Puerto Rico Sea Grant report (Natural Disaster Research, 2001) used both traditional cumulative runup-frequency statistics and rank-order statistics (Sornette *et al.*, 1996) derived from hydrodynamic modeling for calculating wave heights at Aguadilla, Puerto Rico. Included in this Sea Grant report were 1% annual probabilities of exceedance (i.e., according to the FIRM specification) as well as a specification of the 10% probability of exceedance in 50 years.

Geist and Parsons (2005) recently expanded these efforts by comparing empirical analysis of tsunami probabilities with computational PTHA. For a site such as Seaside that lacks an extensive historic record of tsunamis, computational PTHA provides a valuable tool for assessing tsunami risk. For the Cascadia region, Geist and Parsons (2005) compare end-member models of earthquake magnitude distributions: characteristic and Gutenberg-Richter. The latter involves a Monte Carlo simulation where hypocentral location and slip distribution is randomized in the process of building a tsunami hazard curve (tsunami amplitude vs. probability). They also compare an empirical estimate of far-field probabilities with the computational PTHA estimates for local tsunamis. For this study, tsunamis from a characteristic M ~ 9 Cascadia earthquake are part of the PTHA for the Seaside pilot study.

The PTHA methods described in these previous studies are expanded for the Seaside tsunami pilot study to develop, for the first time, a probabilistic tsunami inundation map. In this case, rather than calculating a hazard curve for a point on the coastline, a high-resolution grid is developed for the region around Seaside (see Section 3, "Development of GIS Database") and a hazard curve is computed for each grid cell. For each grid cell hazard curve, the exceedance wave heights for the 1% and 0.2% annual probabilities are interpolated and the results mapped using GIS software.

5.1.2   Application of PTHA to FIRM specifications

The central point in developing the PTHA maps is determining the joint recurrence rate for different sources of tsunamis. This problem has been previously addressed in the development of FIRMs near the mouth of a river where there is combined riverine and coastal flooding as described in a Tetra Tech Inc. report (1981) to FEMA. If riverine flooding at a given elevation (η) occurs at an average recurrence rate of $1/m$ and coastal flooding at η occurs at an average recurrence rate of $1/n$, then the joint recurrence rate is simply $\frac{1}{q} = \frac{1}{m} + \frac{1}{n}$. We can think of this in terms of probabilities such that

$$P_{\text{river}}(\eta, T) = 1 - \exp\left(-\frac{1}{m}T\right) \tag{5.1}$$

and

$$P_{\text{coastal}}(\eta, T) = 1 - \exp\left(-\frac{1}{n}T\right) \tag{5.2}$$

where P is the Poisson, time-independent probability of exceedance and T is the exposure time.

The combined probability from both sources of flooding is given by

$$P(\eta, T) = 1 - (1 - P_{\text{river}})(1 - P_{\text{coastal}}) = 1 - \exp\left[-\left(\frac{1}{m} + \frac{1}{n}\right)T\right] \tag{5.3}$$

Thus, the apparent recurrence rate for the combined source is $\frac{1}{m} + \frac{1}{n}$. A similar approach to determine the probability of ground shaking from multiple sources is described by Ward (1994).

We can adopt the same methodology (Tetra Tech Inc., 1981) to determine the joint recurrence rate for multiple tsunami sources. Suppose that in a given source region (with position vector $\mathbf{r_0}$), we can determine the rate at which a tsunamigenic source with source parameter set (ψ_s) occurs: $\dot{n}(\mathbf{r_0}, \psi_s)$. Typically, in PTHA the objective is to determine the total rate $\dot{N}(\mathbf{r}, \eta_{\text{crit}})$ at which wave height exceeds a risk tolerance value (η_{crit}) at a specific coastal site ($\mathbf{r}$). In general, this involves a double integral over the parameter space for a given source and over all source locations (for example, Anderson and Brune, 1999; Ward, 2001):

$$\dot{N}\left(\mathbf{r}, \eta_{\text{crit}}\right) = \int\limits_{A} \int\limits_{\psi_s^{\text{crit}}(\mathbf{r}, \mathbf{r_0})} \dot{n}\left(\mathbf{r_0}, \psi_s\right) d\psi_s \, dA\left(\mathbf{r_0}\right) \tag{5.4}$$

For our probabilistic inundation map at Seaside, the source locations will include far-field tsunamis from major subduction zone segments around the Pacific and local sources near Seaside. Focusing first on the far-field sources, for a given subduction zone there will be a range of source locations (for example, a $M = 8.0$ earthquake could happen anywhere along the subduction zone), tsunamigenic magnitudes, and recurrence intervals. For a range of tsunamigenic earthquake magnitudes ($M_{\text{low}} < M < M_{\text{max}}$), each magnitude will be associated with an average recurrence rate according to the Gutenberg-Richter relationship $\log(\dot{n}(\text{M})) = a - bM$, where a and b are empirical constants. M_{low} is the lower cutoff magnitude that would produce a significant tsunami at

Seaside. M_{max} is the maximum earthquake magnitude that can occur along a particular subduction zone or subduction zone segment.

Ideally, we would like to produce many inundation maps for a range of earthquake magnitudes $M_{\text{low}} - M_{\text{max}}$ for each subduction zone. We note, however, that if we just estimate the M_{max}-recurrence pair for each subduction zone, this will provide adequate constraint for high recurrence rate-low wave height tsunamis (that is, $P > 0.01$). Additional inundation runs for smaller magnitude earthquakes will not significantly constrain the $P = 0.01$, $P = 0.002$ exceedance wave heights. The possible exceptions are smaller earthquakes $M < M_{\text{max}}$ in the Prince William Sound segment of the Aleutian-Alaska Subduction Zone that are optimally oriented in terms of wave focusing at Seaside. It is possible that these earthquakes can produce larger tsunamis than M_{max} earthquakes along other subduction zones. M_{max}-recurrence pairs are specified for adjacent regions along all subduction zones considered. For each earthquake source specification, an inundation map is produced. The production of inundation maps for these far-field sources is facilitated by the fact that NOAA/PMEL has pre-computed the open-ocean tsunami wavefield for these sources as part of the FACTS database. Uncertainty in recurrence rates and M_{max} is discussed in the Section 8, "Results."

Once a set of far-field and local inundation maps are prepared, Fig. 12 illustrates how we can determine the 1% annual probability inundation line, using GIS software. To create a map, a hazard curve is calculated for each (x, y) point. As shown below, the tsunami hazard curve plots cumulative frequency of exceedance (ordinate) as a function of exceedance wave height (abscissa). The exceedance wave height incorporates the combined tidal and tsunami wave heights as described in Appendix E. Aggregating the results from all of the inundation runs, at each (x, y) point there would be discrete values plotted in wave height/recurrence rate space. This is shown graphically in Fig. 12, where a hazard curve is derived from all of the inundation runs at each (x, y) point. A regression analysis is run to fit a straight or other parametric line to determine each of these hazard curves. The wave height corresponding to the 0.01 yr^{-1} recurrence rate is determined from the hazard curve at each (x, y) point and contoured over x-y space to produce a probabilistic exceedance wave-height map. A similar procedure is used to also produce the 0.002 yr^{-1} exceedance wave-height map.

PTHA can also accommodate a comprehensive treatment of uncertainties in much the same way as PSHA (Senior Seismic Hazard Analysis Committee (SSHAC), 1997). For convenience, two types of uncertainty are often considered: aleatory and epistemic. In simple terms, aleatory uncertainty is often associated with the natural complexity of the physical process itself, whereas epistemic uncertainty is associated with incomplete knowledge about the physical process that can be lessened through the collection of additional data. Aleatory uncertainty is sometimes called external, objective, random, or stochastic uncertainty, whereas epistemic uncertainty is sometimes called internal, subjective, or functional uncertainty (National Research Council (NRC), 2000). A comprehensive treatment of uncertainty requires scientific guidance from a broad range of scientific experts. In the past, this has been performed through a Technical Integrator or Technical Integrator/Facilitator (Senior Seis-
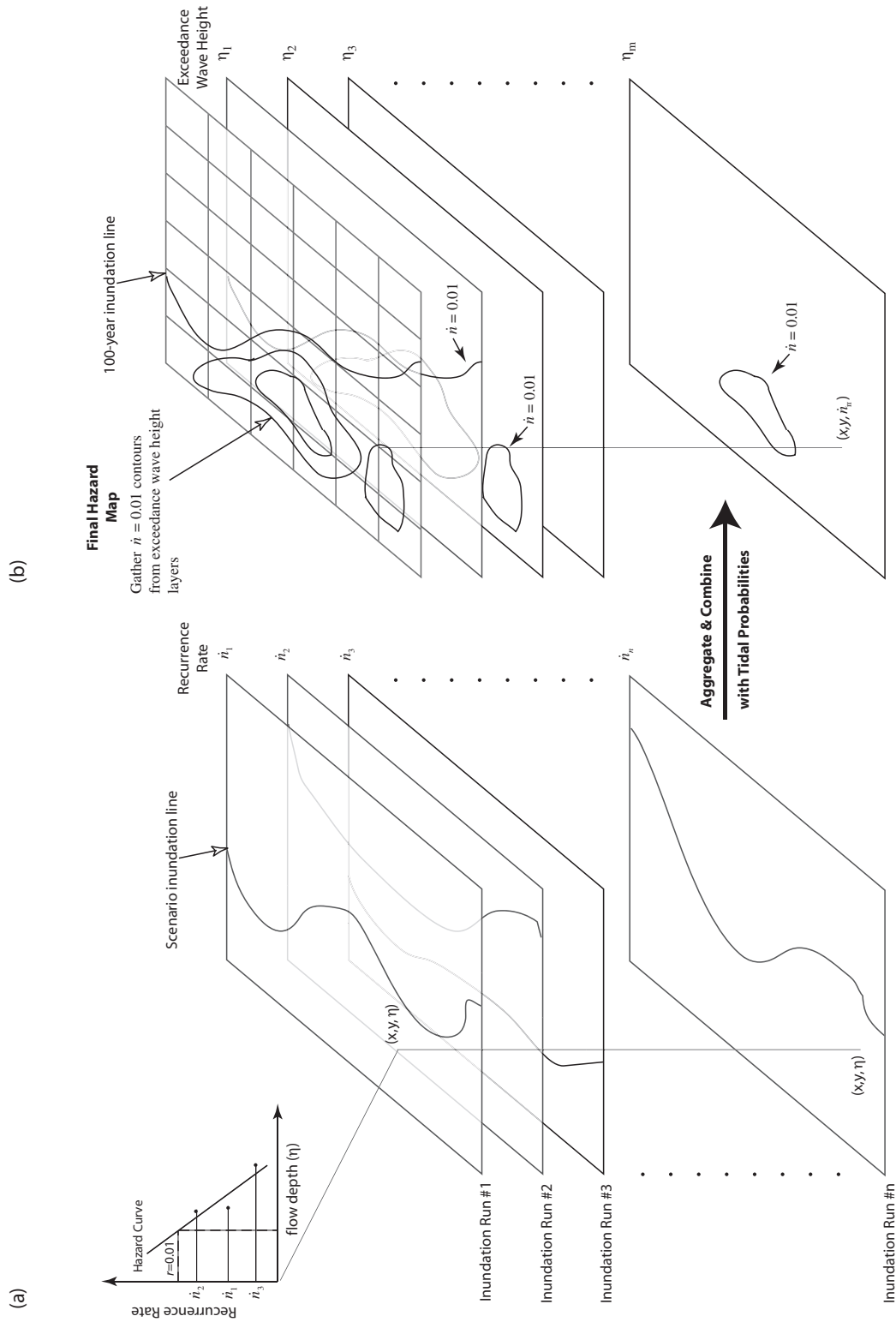
Figure 12: General procedure for developing probabilistic tsunami hazard map of exceedance wave height for the 0.01 yr^{-1} recurrence rate. (a) Inundation runs for each source are associated with a particular recurrence rate (i.e., earthquake probability). (b) All inundation runs in (a) are aggregated and combined with tidal probabilities (Appendix E) to produce maps of contoured recurrence rate for a given exceedance wave height (only 0.01 yr^{-1} rate contour shown for each layer). Final hazard map produced by gathering contours of a particular rate from exceedance wave height layers (Appendix G).

mic Hazard Analysis Committee (SSHAC), 1997) process that determines the "legitimate range of technically supportable interpretations" and "the relative importance or credibility that should be given to the differing hypotheses across that range."

For this preliminary study, however, we focus on including those uncertainties that are readily quantifiable. These are primarily aleatory uncertainty of tsunami arrival time relative to the tidal stage (Appendix E) and the slip distribution of the earthquake. The only epistemic uncertainty we consider is the two earthquake models for the Aleutian-Alaska Subduction Zone set forth by Wesson *et al.* (1999). We compare the probabilistic results using different rupture models and estimates of recurrence rates for a local Cascadia earthquake, but do not explicitly include this uncertainty in the probabilistic calculations. Other possible sources of epistemic uncertainty are indicated in Section 9, "Discussion," of this report, but not included in this study. To include these sources of uncertainty would require the assignment of relative weights in a logic-tree approach and hence, the consensus among a wide range of scientific experts. It is recommended that the level of uncertainty analysis be related to the specific objectives of the probabilistic study as described in Section 3 of the SSHAC (1997) report entitled "Structuring and Implementing a PSHA."

5.2   Source Specification

5.2.1   *Source magnitude and geometry*

5.2.1.1   Typical interplate thrust earthquakes

Earthquake source parameters used in this study include primarily the largest earthquakes (that is, $M = M_{max}$) along major north Pacific Subduction Zones and the southern Chile Subduction Zone, site of the 1960 M = 9.5 earthquake and trans-oceanic tsunami. The rationale for choosing the largest earthquakes is that, even though the recurrence rate for each event is low, when combined these earthquakes (along with local Cascadia earthquakes) should be sufficient to specify the tsunami at Seaside from *any source* with an average return time of 100 years and 500 years. Inclusion of smaller magnitude and more frequent earthquakes will likely not add significantly more information with which to constrain the 100-year exceedance wave heights. The exception is inclusion of smaller earthquakes in the Prince William Sound segment of the Aleutian-Alaska Subduction Zone, that can result in larger runup values than $M = M_{max}$ earthquakes in other subduction zones. In using this set of source parameters, it will appear that we are adopting a characteristic earthquake distribution model (Appendix F). This may be the case, for example, in the 1964 Alaska source region. In most cases, however, we are choosing an earthquake magnitude that is at the extreme tail of a continuous distribution of earthquake magnitudes (that is, that of a modified Gutenberg-Richter distribution; see Appendix F).

The primary source parameters that are provided are magnitude, width, length, and slip. Because we are relying on pre-computed solutions from NOAA/PMEL's FACTS database for the far-field sources, it is assumed that other source parameters such as depth, dip, strike, and slip direction have already been determined from the best available sources. Except for local events, it will be assumed that variations in slip distribution patterns from event to event will have minimal effect on far-field tsunami amplitudes (see Titov *et al.*, 1999). Wherever possible, published references will be provided for estimates of these source parameters. It should be noted, however, that for the objectives of the probabilistic study, these source parameters will not be based strictly on historic events but on events that are thought to be representative of the $M = M_{\mathrm{max}}$ earthquake for each subduction zone. Average earthquake return times may be cited for different cases, though it is important to note that these are estimates subject to epistemic uncertainty. The Alaska-Aleutian, Kamchatka, Kuril, and southern Chile Subduction Zones are discussed in the sections below.

Table 6 below summarizes the earthquake source parameters and recurrence rates used in this study. Horizontal dimensions have been adjusted according to the pre-set parameters in the FACTS database constrained by the seismic moment relationship. Details of each source region are given in the next section.

5.2.2   Far-field earthquakes

5.2.2.1   Alaska-Aleutian Subduction Zone

Because the probabilistic tsunami hazard assessment for the Tsunami Pilot Study closely follows similar efforts used in the National Seismic Hazard Mapping Program, it is judicious to take advantage of previous work in determining likely source parameters. The seismic hazard maps for Alaska are described by Wesson *et al.* (1999). They consider two hazard models (I and II) for the Alaska-Aleutian megathrust: Model I consists of a western and an eastern seismic zone in which earthquakes as large as M = 9.2 can occur. The delineation between the zones occurs approximately at the site of the 1946 Aleutian earthquake. Model II consists of a western Aleutian seismic zone (Zone A) as in Model I, but a smaller eastern Alaska seismic zone (Zone C) with a western boundary coincident with the rupture boundary for the 1964 earthquake.

Because the intervening zone (Zone B) that includes the Shumagin seismic gap (Nishenko, 1991) and the source area for the 1938 earthquake can only accommodate earthquakes up to magnitude 8.5, there is a saddle (low region) in the expected seismic hazard near Zone B. For the purposes of far-field tsunamis, Model I is probably more representative of the long-term zonation for large earthquakes. Near the source region for the 1964 earthquake, paleoseismic studies indicate that return times of great earthquakes is roughly 600–800 years (Combellick, 1992; Gilpin and Carver, 1992; Wesson *et al.*, 1999). Average return times for M = 9.2 earthquakes along the Aleutian part of the subduction zone are probably similar, but more work is needed to constrain these times. The tsunami models for the largest earthquakes would closely

Table 6: Source specification for earthquakes used in this study.

Source Number	Location	M	Length (km)	Width (km)	Slip (m)	Mean Inter-event Time (yr)	FACTS Specification
1	Alaska-Aleutian	9.2	1000	100	17.7	1,313	A0–A9 & B0–B9 (Tsunami model 1—western zone)
2	Alaska-Aleutian	9.2	1100	100	18.1	750	A9–A19 & B9–B19 (Tsunami model 1—mid source)
3	Alaska-Aleutian	9.2	600	100	—	750	Distributed slip: 15 m ⋆ (A20+B20) + 20 m ⋆ (A21+B21) + 25 m ⋆ (A22+B22) + 30 m ⋆ (A23+B23+A24+B24) (Tsunami model 1—eastern zone)
4	Alaska-Aleutian	9.2	1200	100	16.3	1,133	A0–A11 & B0–B11 (Tsunami model 2—western zone)
5	Alaska-Aleutian	9.2	1200	100	14.8	750	A12–A23 & B12–B23 (Tsunami model 2—western zone)
6	Alaska-Aleutian	8.2	300	100	2.1	875	A17–A19 & B17–B19
7	Alaska-Aleutian	8.2	300	100	2.1	661	A20–A22 & B20–B22
8	Alaska-Aleutian	8.2	300	100	2.1	661	A23–A25 & B23–B25
9	Kamchatka	8.8	500	100	9.8	100	A1–A5 & B1–B5
10	Kamchatka	8.8	500	100	9.8	100	A6–A10 & B6–B10
11	Kuril	8.5	300	100	5.8	500	A11–A13 & B11–B13
12	Kuril	8.5	300	100	5.8	500	A14–A16 & B14–B16
13	Kuril	8.5	300	100	5.8	500	A17–A19 & B17–B19
14	Southern Chile	9.5	1000	100	40.0	300	A35–A45 & B35–B45
15–26	Cascadia	9.1	Var.	Var.	Var.	520	High-resolution fault model (Flück *et al.*, 1997)

follow the seismic Model I above. The first tsunami model consists of three M = 9.2 earthquakes, with adjacent rupture areas as shown in Fig. 13. One of the M = 9.2 ruptures would correspond in location to the 1964 rupture, whereas the other two rupture areas would not correspond to any historic event. The middle event also spans what some may believe is a tectonic segment boundary at the tip of the Alaska Peninsula. It is important that the rupture areas for the three events do not overlap—this would violate an important seismic moment balance along the subduction zone.

For the purpose of accounting for radiation pattern changes with along-strike shifts of the rupture area (see Fig. 2, gage 3 in Titov *et al.*, 1999), Tsunami Model 2 is introduced with two M = 9.2 earthquakes (Fig. 14). The western rupture area approximately corresponds to the 1957 rupture area, whereas the eastern rupture spans the 1946, 1938, and the western part of the 1964 rupture area. Tsunami Models 1 and 2 are weighted (50% each) and combined to form a composite model. The result would be combined as separate, weighted branches of a logic tree. For each of Models 1 and 2, we are operating under the
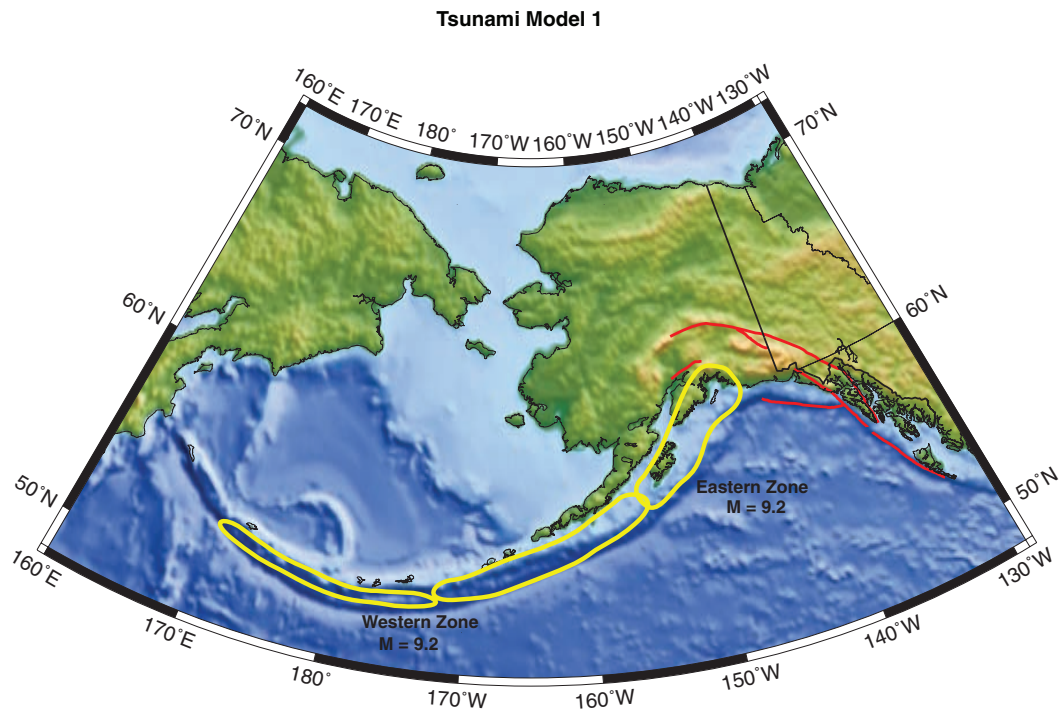
Tsunami Model 1

Figure 13: Model 1 for location of M = 9.2 earthquakes along the Aleutian-Alaska Subduction Zone. Red lines: faults with predominantly strike-slip motion.
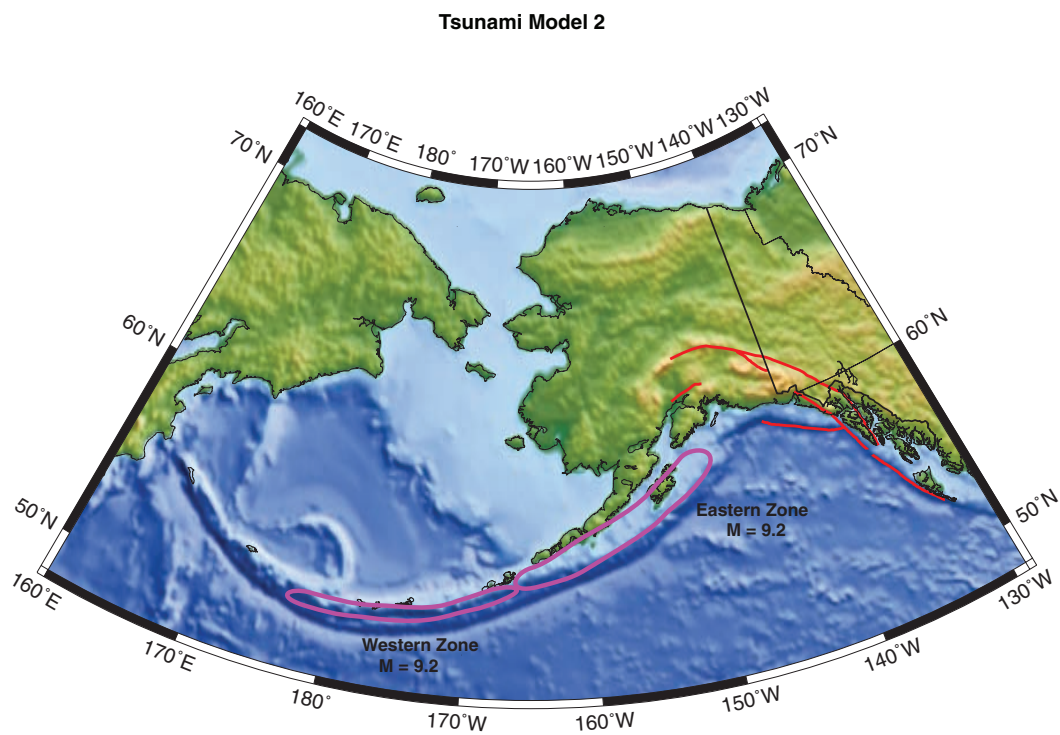
Tsunami Model 2

Figure 14: Model 2 for location of M = 9.2 earthquakes along the Aleutian-Alaska sbuduction zone. Red lines: faults with predominantly strike-slip motion.
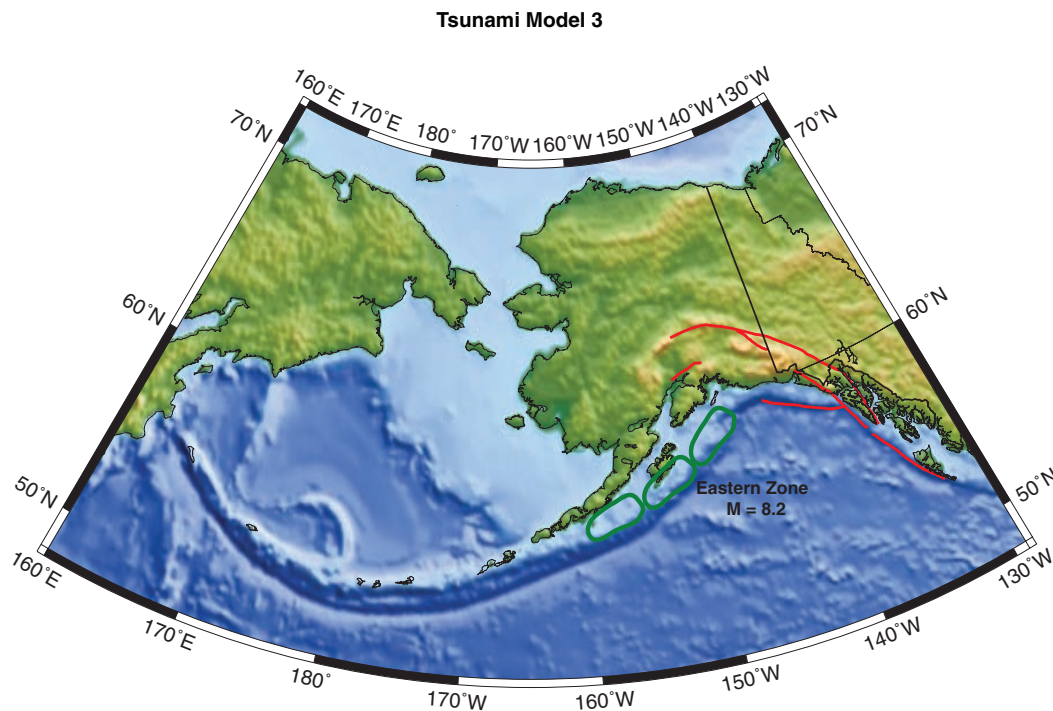
Tsunami Model 3

Figure 15: Model 3 for location of M = 8.2 earthquakes along the Aleutian-Alaska Subduction Zone in the Prince William Sound region. Red lines: faults with predominantly strike-slip motion.

hypothesis that large earthquakes (and even small earthquakes; Tanioka and González, 1998) will rupture across segment boundaries defined by tectonic and geologic structures.

Finally, to accommodate the possibility that a smaller magnitude earthquake (M = 8.2) in Prince William Sound may cause larger inundation at Seaside than other earthquakes considered in this initial set of source parameters, a third tsunami model (Fig. 15) is included that consists of three adjacent M = 8.2 ruptures, similar to the 1938 rupture. The recurrence rates for the M = 8.2 ruptures are again derived from Wesson *et al.* (1999).

For the Alaska-Aleutian Subduction Zone, eight inundation runs have been completed: three for Model 1, two for Model 2, and three for Model 3.

5.2.2.2 Kamchatka Subduction Zone

Like the Alaska-Aleutian Subduction Zone, large earthquakes have occurred along the Kamchatka Subduction Zone (KSZ) with noticeable frequency. Pinegina *et al.* (2003) recently concluded that Kamchatka has been impacted by large tsunamis at a rate of 1 every 100 years for the past 3,000 years, though not all are from local sources (~10–20% far field). Of note, the M_w = 8.8 1952 (Johnson and Satake, 1999) and the M_t = 8.8 1923 (Abe, 1979) earthquakes are probably representative of the largest earthquakes of this subduction zone. A tsunami model for Kamchatka can be constructed as done for the Alaska Tsunami Model 1 above, where two adjacent M = 8.8 earthquakes fill the entire subduction zone.

5.2.2.3 Kuril Subduction Zone

Continuing south along the Kuril Subduction Zone, the maximum magnitude earthquake is likely to be slightly smaller than for the Kamchatka Subduction Zone, primarily because of a change in tectonic regime for the overriding plate. From the analysis of the 13 October 1963 Kuril Islands earthquake (there was also a tsunami earthquake in the Kuril Islands on 20 October 1963) which Ward (1982) and Ruff and Kanamori (1983) placed at $M_w = 8.5$ and recent evidence of multi-segment rupture in the southern part of the Kuril Subduction Zone by Nanayama *et al.* (2003), it is reasonable to characterize this subduction zone with a series of M = 8.5 earthquakes. Nanayama *et al.* (2003) indicates that the average return time for these earthquakes is approximately 500 years. Approximately three M = 8.5 earthquakes would fill the Kuril Subduction Zone up to the southern extent of the Kamchatka Subduction Zone.

5.2.2.4 Southern Chile Subduction Zone

Earthquakes along the Chilean Subduction Zone are also considered, primarily because of the size of the M = 9.5–9.6 1960 earthquake (Cifuentes, 1989; Cifuentes and Silver, 1989) and observations of the associated tsunami along the west coast of North America. The amount of slip that occurred during the 1960 tsunami is difficult to ascertain because of the complexity of the event. The geodetic models of both Linde and Silver (1989) and Barrientos and Ward (1990) result in average amounts of slip that correspond to significantly lower seismic moment estimates than determined from seismic waveform data, though still at a M ~ 9.5 level. Average slip estimates vary from 17 m to 20 m, though the variable slip models indicate significantly higher amounts of slip, as much as 40–50 m, are predicted for the offshore extent of rupture and even small earthquakes (Barrientos and Ward, 1990; Linde and Silver, 1989). For comparison, Liu *et al.* (1995) use 24 m of slip in their far-field tsunami model.

Chile has been struck by giant earthquakes and tsunamis in the past, including the 1570s, 1730s, 1837, and the M ~ 9.5 1868 earthquake in northern Chile. These dates are not representative of return times for M ~ 9.5 earthquakes from purely a moment-balance perspective (Barrientos and Ward, 1990) and from recent paleoseismologic analysis by Salgado *et al.* (2003). The latter study suggests an average return time for great earthquakes in Chile of ~250 years. Even so, if the average slip per event is ~20 m, this results in a seismic slip rate of 8 cm/yr—close to the relative plate convergence rate of 8.4 cm/yr. Although the southern Chile Subduction Zone is considered the most highly coupled subduction zone in the world in terms of seismic efficiency (Scholz, 1990), the repeat time should not be much smaller, nor the average slip per event be much greater, than these estimates to satisfy the moment balance.

5.2.3 Cascadia Subduction Zone earthquakes

This part of the pilot study is of particular importance because M ~ 9 earthquakes along the Cascadia Subduction Zone will likely produce the worst-case

tsunami inundation and be the defining event for the 500-year tsunami flood standard. We first discuss how the coseismic displacement field can be calculated for variable slip (Geist, 2002), building on previous inundation mapping efforts (Priest *et al.*, 1997). Not only does the coseismic displacement field provide the initial conditions for tsunami propagation, but it will also affect inundation estimates because of coseismic subsidence of coastal regions. We will then discuss different approaches to incorporating uncertainties caused by incomplete knowledge of rupture geometry and by different slip distribution patterns into the probabilistic calculations. Discussion of recurrence rates and time-dependent probability calculations is presented by Petersen *et al.* (2002).

5.2.3.1 Specification of Cascadia earthquake magnitudes

There is mounting evidence that the last major Cascadia Subduction Zone earthquake in the year 1700 had a magnitude approximately equal to M ~ 9 (Satake *et al.*, 2003). Available paleoseismic data indicate that other major earthquakes have struck the Cascadia margin, though it is unclear whether these earthquakes were "characteristic" M = 9 events or whether they also included smaller magnitude earthquakes. The method that the National Seismic Hazard Mapping program employed to characterize earthquakes along the interplate thrust was to use two equally weighted scenarios: (1) a M = 9.0 characteristic earthquake with an average repeat time of 500 years and (2) a series of M = 8.3 earthquakes that fill the seismogenic region of the interplate thrust every 500 years, resulting in a repeat time of 110 years for a M = 8.3 earthquake to occur anywhere in the seismic zone (Frankel *et al.*, 1996; Frankel *et al.*, 2002; Petersen *et al.*, 2002). These two scenarios represent epistemic uncertainty that is included in the probabilistic calculations for the seismic hazard maps.

One could now argue, however, that this either/or option has been superseded with recent analysis of the Japan tsunami records that indicate the 1700 event had a magnitude of M = 8.7–9.2 and ruptured approximately 1100 km (Satake *et al.*, 2003). That is, the epistemic uncertainty regarding magnitude posed in the National Seismic Hazard maps has essentially been resolved with the collection of new data (that is, tsunami records in Japan). This does not exclude the possibility of M < 9 earthquakes occurring along the interplate thrust. Instead, the epistemic uncertainty may now be whether the magnitude *distribution* is characteristic or a Gutenberg-Richter (G-R) distribution (Appendix F). Toward this end, Geist and Parsons (2005) consider two end-member cases of a characteristic M = 9 earthquake and a modified G-R distribution of earthquakes for demonstrating methods to calculate tsunami probabilities. Because of a lack of information to define a G-R distribution for the Cascadia Subduction Zone (see Discussion), we focus primarily on M = 9 events as specified by Satake *et al.* (2003) and Leonard *et al.* (2004), though this is certainly a topic open for future research and inclusion in future PTHA studies.

5.2.3.2   Calculation of coseismic displacement field

To calculate the coseismic displacement field, we can take advantage of previous work performed by Priest *et al.* (1997) in developing deterministic tsunami inundation maps. The source discretization currently implemented in FACTS may not be fine enough to accommodate slip pattern variations. Optimally, it is best to modify the fault grid developed by Flück *et al.* (1997) and used by Priest *et al.* (1997). This grid includes 105 quadrilateral elements with varying dip and strike.

The stochastic source model is modified from that of Herrero and Bernard (1994) as described by Geist (2002). In basic terms, the model computes a stochastic slip distribution that conforms to a specific amplitude spectrum in the wavenumber domain that is constrained by earthquake physics and observations. Randomizing the phase spectrum and transforming to the spatial domain yields a wide variety of slip distribution patterns. Scaling constants are adjusted so that the average slip for all slip distributions produced by the model equal the specified seismic moment or independent slip estimates from far-field tsunamis and/or coastal subsidence. The slip distribution then can be mapped to the fault grid without too much distortion of the wavenumber spectrum. It is important to recognize that the stochastic source is specifically designed to estimate the aleatory uncertainty related to slip for a given seismic moment. Any single slip distribution has a low probability of occurring and should not be considered as a characteristic slip distribution (i.e., one which represents the slip distribution for *each* earthquake, with little uncertainty) (cf., Schwartz, 1999). Such a model, not considered here, is tightly constrained by the overall convergence rate and time since the last event.

An important consideration is how to deal with slip in the transition zone (Flück *et al.*, 1997) and uncertainty in the rupture width. In past coseismic displacement studies, slip is assumed to taper in the transition zone from full slip adjacent to the locked zone to zero at the downdip edge of the transition zone (Flück *et al.*, 1997; Leonard *et al.*, 2004). In Satake *et al.* (2003), three long-rupture models are considered for the 1700 C.E. earthquake that are compatible with both the tsunami records and coastal subsidence estimates: a "Long-Narrow" model with uniform slip in the locked zone and slip tapered to zero half-way down the transition zone; a "Long-Splayed" model like the Long-Narrow model, but with a seaward-vergent splay fault at the updip edge of rupture; and a "Long-Wide" model with uniform slip throughout both the locked and transition zones.

Because the Satake *et al.* (2003) study could not resolve between the Long-Narrow and Long-Wide rupture models at a reasonable level of confidence, there is still uncertainty related to the rupture width. The National Seismic Hazard Maps handle this uncertainty by considering five different rupture widths that extend through the transition zone (Petersen *et al.*, 2002). We make the case that uncertainty related to the effective width of the rupture zone is in part aleatory uncertainty associated with slip distribution patterns. The slip distributions used for the local tsunami models are based on the Long-Wide rupture geometry. Using this geometry, regions where slip is concentrated up-dip, for example, will have a narrow effective rupture width. Even so, there

is still a level of epistemic uncertainty related to the region where slip can occur for a Cascadia Subduction Zone earthquake. If we limit variable slip to a narrow zone consistent with the Long-Narrow rupture geometry, mean tsunami amplitudes are larger (Geist, 2005). For this pilot study, we did not consider this latter case.

The uncertainty in rupture width is also related to how well the coastal subsidence predicted using the slip distributions for the local tsunami models compare to the observations. The event for which there are the most abundant paleoseismic observations is the 1700 C.E. earthquake (Leonard *et al.*, 2004). Recognizing that the stochastic slip distributions represent a range of possible rupture modes (i.e., they are not representative of one particular event) and that there is significant uncertainty associated with the paleoseismic subsidence measurements themselves, most of the slip distributions tend to over-predict subsidence in comparison to the estimates from the 1700 C.E. earthquake (Leonard *et al.*, 2004). There are, however, *individual* slip distributions that provide an adequate comparison to the observed subsidence observations. Moreover, reductions in rupture width as little as 12.5% (still greater than the Long-Narrow geometry) greatly reduce the subsidence predictions. Thus, for the Cascadia geometry, coastal subsidence is more sensitive to uncertainty in rupture width than average slip. Tsunami generation, on the other hand, is more sensitive to average slip and slip distribution.

Finally, we estimate how many model runs it may take to capture that natural variability in runup heights caused by variations in slip distribution patterns. To do this, we track variation in peak nearshore tsunami amplitude (PNTA) at the 100 m isobath, which can be quickly computed using linear propagation models. In Fig. 16, both the standard deviation of PNTA (blue) offshore Seaside and the difference between maximum and minimum PNTA values (magenta) are shown as a function of the number of model runs. As is typical with this type of computational effort, representational gains in modeling the physical system die off exponentially with the number of model runs. In this case, a minimum of about 12 model runs would be needed to capture the natural variability in PNTA.

5.2.3.3 Specification of earthquake recurrence rates

In the Cascadia region, numerous paleoseismic investigations have been conducted to determine the recurrence record of great earthquakes (for example, Atwater and Hemphill-Haley, 1997; Atwater *et al.*, 2004; Kelsey *et al.*, 2002; Witter *et al.*, 2003). In this section, we show how empirical parameters that define the regional probability distributions can be determined, taking into account uncertainty in age-dating methods and the open time intervals before the first and after the last earthquake dated in the geologic record (Ogata, 1999). We also show how the method for determining empirical distribution parameters can be applied directly to establishing tsunami probability distributions.

The age range of geologic horizons representing great earthquakes is a result of dating samples from multiple sites, each with an associated uncertainty related to the age dating technique used. These age ranges, as well as open intervals before the first and after the last geologic horizon and a
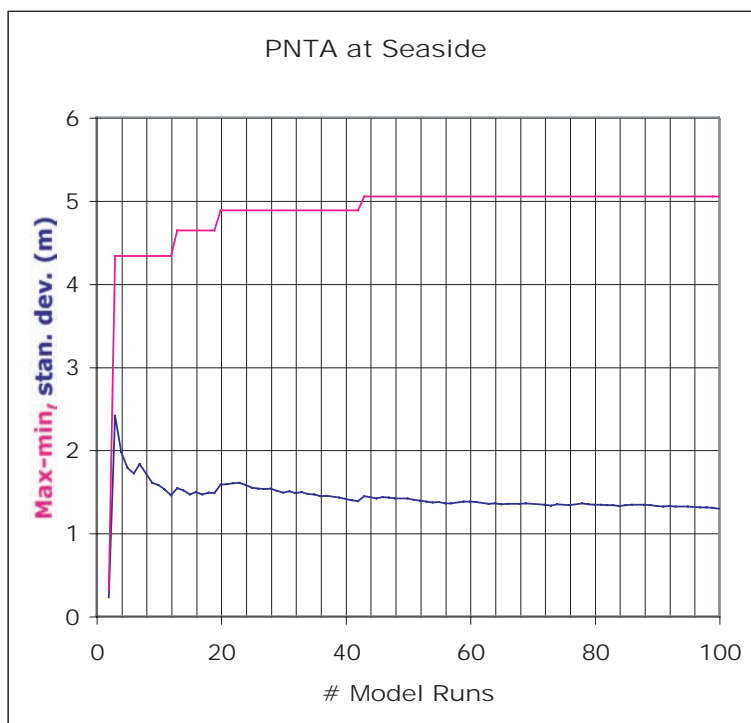
Figure 16: Level of variability in peak nearshore tsunami amplitudes (PNTA) offshore Seaside as a function of the number of stochastic slip distributions used. Pink: difference in maximum and minimum values of PNTA. Blue: standard deviation of PNTA values.
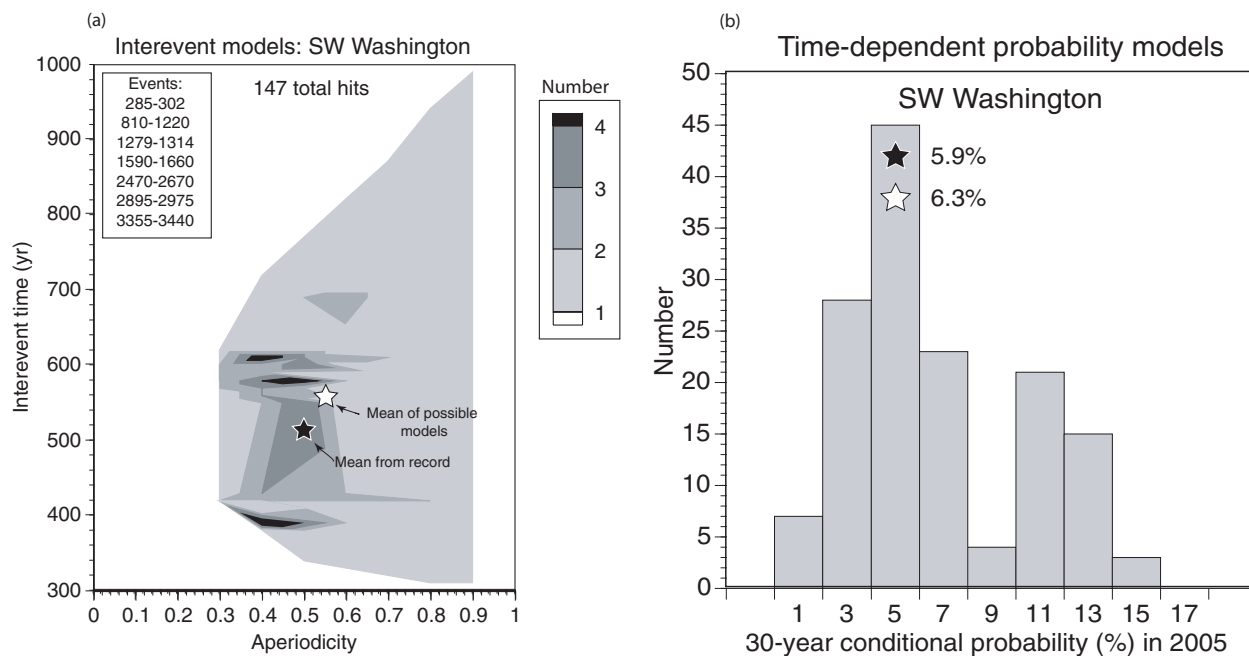

Figure 17: Results of Monte Carlo analysis of inter-event times and aperiodicity, using paleoseismic horizons identified and dated by Atwater *et al.* (2004).

limited sampling of earthquake recurrence history, introduce uncertainty in determining the mean inter-event time and aperiodicity. To determine the range of distributions that are consistent with available paleoseismic data, a Monte Carlo simulation is performed in which a random sample of earthquake times is drawn from a specified probability distribution with varying mean inter-event times (μ) and aperiodicities (α) (Parsons, 2004, submitted). Either mean values of μ and α for all random samples that fit the observations can be used, or a range of values can be carried through the probability calculations enabling an estimate of parameter sensitivity.

Results using paleoseismic data from southwest Washington (Atwater *et al.*, 2004) are shown in Fig. 17. The event table shows the age ranges (calibrated years B.P.) for the identified horizons and the plots show the successful distributions defined in μ-α parameter space that produce hits in the age ranges for the events. The histogram shows the 30-year conditional probability resulting for all successful hits, using the Brownian Passage Time probability distribution (Matthews *et al.*, 2002). The probability corresponding to the mean of the successful hits is shown by the white star (μ = 566 years, α = 0.55).